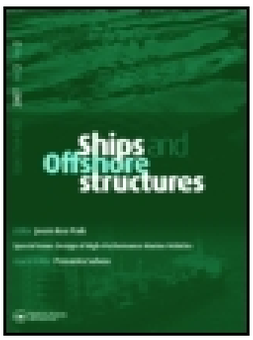

Taylor & Francis
Taylor & Francis Group

Ships and Offshore Structures

ISSN: (Print) (Online) Journal homepage: https://www.tandfonline.com/loi/tsos20

Thermal analysis of marine structural steel EH36 subject to non-spreading cryogenic spills. Part II: finite element analysis

Mojtaba Mokhtari, Woongshik Nam & Jørgen Amdahl

To cite this article: Mojtaba Mokhtari, Woongshik Nam & Jørgen Amdahl (2021): Thermal analysis of marine structural steel EH36 subject to non-spreading cryogenic spills. Part II: finite element analysis, Ships and Offshore Structures, DOI: 10.1080/17445302.2021.1979920

To link to this article: https://doi.org/10.1080/17445302.2021.1979920

Published online: 02 Oct 2021.

SHIPS AND OFFSHORE STRUCTURES
https://doi.org/10.1080/17445302.2021.1979920

Thermal analysis of marine structural steel EH36 subject to non-spreading cryogenic spills. Part II: finite element analysis

Mojtaba Mokhtari, Woongshik Nam and Jørgen Amdahl

Centre for Autonomous Marine Operations and Systems (AMOS), Department of Marine Technology, Norwegian University of Science and Technology (NTNU), Trondheim, Norway

ABSTRACT

In Part I of this paper, six liquid nitrogen (LN_2) pool boiling tests were carried out to locally cool down six different EH36 steel plates to cryogenic temperatures. Leindenfrost and Critical Heat Flux (CHF) points of LN_2 boiling curve were estimated. These estimations together with the recorded temperature histories are used in this part for the development of a heat flux curve for EH36 steel-LN_2 pool boiling through Finite Element Thermal Analysis (FETA) of the problem investigated experimentally in Part I. Thermal conductivity and heat capacity of EH36 are defined by two unprecedented temperature functions based upon experimental studies in cryogenic temperatures. A user subroutine written in FORTRAN defines the air convection coefficient as a function of surface-air temperature difference, which changes with time and location. Results of this study contribute to the Accidental Limit State (ALS) design of marine and offshore structures for liquified gas spill scenarios.

ARTICLE HISTORY
Received 12 May 2021
Accepted 7 September 2021

KEYWORDS
Cryogenic spill; marine steel; offshore; numerical; heat transfer; boiling

Nomenclature

α	thermal diffusivity (mm^2/s)
c_p	specific heat capacity (J/kg-K)
h	convection coefficient (W/m^2-K)
κ	thermal conductivity (W/m-K)
q	heat flux (W/m^2)
T	temperature (°C)
ΔT	temperature difference between fluid and steel surface
t	time (s)
ρ	density (kg/m^3)

Subscripts

a	air
bs	bottom surface
gp	grip part
s	surface (steel plate surface)
ts	top surface

Acronyms

ALS	Accidental Limit State
CFD	Computational Fluid Dynamics
CHF	Critical Heat Flux
FEA	Finite Element Analysis
FETA	Finite Element Thermal Analysis
HAZ	Heat Affected Zone
LN_2	Liquid Nitrogen
LNG	Liquified Natural Gas
ONB	Onset of Nucleate Boiling

1. Introduction

In Part I of this paper (Nam et al. 2021), it was explained that the accidental release of Liquefied Natural Gas (LNG) on marine and offshore structures may cause steel to embrittle in cryogenic temperatures. The combination of steel embrittlement and tensile thermal stresses could lead to a brittle fracture and even a catastrophic failure of the structure. Therefore, for a safer Accidental Limit State (ALS) design of ships and offshore structures, it is necessary to accurately predict their performance in cryogenic conditions.

Thus far, a number of experimental and numerical studies have investigated the structural performance of offshore structures and ships in low or cryogenic temperatures (Ehlers and Østby 2012; Nam et al. 2018; Paik et al. 2020). In these studies, uniform temperature, was applied throughout the structure (i.e. no temperature gradient was considered). However, in the event of liquified gas leakage, it is likely that only a limited part of the structure comes in contact with the cryogenic liquid which induces thermal stresses in the structure. Such thermal stresses could cause local failures involving one or more components, which in turn may lead to the global collapse of the structure. Therefore, it is important to investigate the thermal-structural performance of steel structures with local areas subject to cryogenic cooling. The structural response of such structures is highly dependent on the temperature field and the thermal gradient. The temperature field should be obtained from a transient heat transfer analysis which is lacking in the literature. Therefore, the present study aims to address this gap and establish a foundation for the transient heat transfer analysis of marine steel structures subject to cryogenic spills.

This paper focuses on the Finite Element Thermal Analysis (FETA) of the pool boiling tests presented in Part I (Nam et al. 2021). The structural response of the plate specimens will be presented in a separate paper in the near future. In FETA, values adopted for thermophysical properties of the steel, the cryogenic liquid, and the ambient air significantly influence the temperature field and the thermal gradient in the structure. Hence, eight sensitivity analyses were carried out in this study to shed light on the impact of associated uncertainties on the FETA results.

CONTACT Mojtaba Mokhtari mojtaba.mokhtari@ntnu.no

2. Pool boiling tests

Six pool boiling tests were conducted in Part 1 (Nam et al. 2021), which are briefly explained in this section. The liquid pools were built on six different specimens that were cut from 8 mm thick EH36 steel plates with the dimensions illustrated in Figure 1. Two specimens (PLATE #1 and PLATE #2) were cut parallel, and another two (PLATE #3 and PLATE #4) perpendicular, to the plate rolling direction. For the last two specimens (PLATE #5 and PLATE #6), two 400 mm × 560 mm plate pieces were fused together by butt welding to investigate the influence of welding and heat-affected zone (HAZ) on the thermal and structural behaviour of the plate exposed to cryogenic spills. The experimental set-up was aimed to replicate the thermal-structural behaviour of unstiffened marine steel plates with a fatigue crack in a non-spreading LNG spill scenario. However, the structural behaviour of the steel plates is out of the scope of this study, and only the thermal results were discussed.

To develop the fatigue crack in the specimens, a through-thickness crack was machined at the centre of all specimens. Then, fatigue cracks were created by applying tensile cyclic loading. Eight thermocouples were placed on the bottom surface of each specimen as shown in Figure 1 to record the temperature histories across the specimens. One additional thermocouple (T9) was placed in the air, 20 mm below the bottom surface, to measure the ambient temperature near the plate during the tests. No thermocouple was situated at the plate centre due to the existing crack.

Liquid nitrogen (LN_2) was used as the cryogenic liquid owing to its similar thermophysical properties to LNG. A container with dimensions of 250 mm × 250mm × 70mm was positioned at the centre of each specimen. The container was built from four aluminium plates and the corners were sealed with thermally conductive and non-corrosive silicone with excellent adhesion to prevent the leakage of LN_2. Aluminium tape was also used at all corners including those between the steel surface and the walls to prevent direct contact between silicone and the cryogenic liquid. Closed-cell foams covered the external surface of aluminium plates (container walls) to avoid heat transfer from the air to the liquid pool through the walls. The hole in the centre of each specimen caused by the artificial crack was also sealed with aluminium tape to prevent LN_2 leakage.

Before starting each pool boiling test, an initial 100 kN tensile load was applied to the specimen by a hydraulic actuator. Tensile stresses in the specimen increased during the pool boiling tests due to the contraction of specimens until cleavage fracture occurred. In a few cases where the contraction was not enough to cause a fracture, the fracture was achieved by increasing the external load. The hydraulic actuator was connected to the specimen through test jigs designed and fabricated exclusively for the specimens of this study. To connect the specimen to the test jigs, 10 holes with a diameter of 49 mm were machined near its right and left edges (five holes at each edge).

3. Finite element modelling

Transient thermal analyses were conducted in this study using the finite element code Abaqus. Due to the symmetry conditions, a quarter model was developed to improve computational efficiency (Figure 2). The finite element models include an EH36 steel plate with six different zones defining six different convective heat transfer conditions. Figure 2 shows the size and the location of these zones. The steel surface inside the pool boundaries was divided into two different zones, Zone #1 and Zone #2, which together simulated the convective heat transfer between the steel surface and the LN_2 pool. Zone #1 simulated direct heat flux to LN_2. Heat transfer between the steel surface and LN_2 in Zone #2 took place indirectly, through the aluminium tape that was used to fix the container and seal the gaps between the container walls and the steel surface. The cooldown time of a surface in contact with a cryogenic liquid has been demonstrated to reduce substantially by placing a thin coating on the surface (Cowley et al. 1962; Allen 1966; Maddox and Frederking 1966; Leonhard et al. 1967). Accordingly, in a sensitivity analysis, an earlier transition from the film boiling to the nucleate boiling was assumed for Zone #2, which is explained in the following section. Zone #3 is the area where the container walls and the closed-cell foams were located. Heat transfer in this zone was considered negligible, and thereby adiabatic surface temperature was adopted. Zones #4 and #6 represent areas where convective heat transfer between the steel surface and the air took place. Zone #5 defines the heat transfer between the steel surface and the grip parts.

3.1. LN_2 heat transfer

LN_2 was used as the cryogenic liquid given its similar thermophysical properties to LNG (see Part I). These similar properties have resulted in comparable heat flux curves for them as shown in Figure 3 (Dabiri 1986; Wuersig et al. 2009; Liu et al. 2015; Barron and Nellis 2017). There are several boiling curves for LN_2 reported in the literature, three of which (Curves I, II and III) have been plotted in Figure 3 to be investigated herein. Most of the boiling curves in the literature were obtained from either pool boiling tests or correlations based upon pool boiling tests, such as those in Baron (Barron and Nellis 2017) and Dabiri (Dabiri 1986). Although all the conventional boiling curves follow the typical boiling regimes shown in Figure 4, they slightly vary typically around Leidenfrost and Critical Heat Flux (CHF) points. The differences between the conventional boiling curves, such as Curves I and II, may appear insignificant, but they are likely to noticeably affect the predictions of numerical heat transfer, in part because these curves have been presented in logarithmic charts. The differences between the reported boiling curves may have stemmed from the uncertainties that influence the heat flux, such as surface roughness, heat transfer from ambient air, ambient temperature, ground/substrate material, temperature-dependent properties of the ground/substrate material, etc.

Recently, attempts have been made to calculate the source term of a cryogenic liquid spill using Computational Fluid Dynamics (CFD) which delivered an approximated boiling curve for LN_2 (Curve III in Figure 3 (Liu et al. 2015)). Although the computational boiling curve follows the typical boiling regimes, it returns significantly different heat flux values for the transition and the nucleate boiling regimes. Regardless of the complexity of the boiling phenomenon and its computational modelling, these significant differences are most likely due to not taking into account some of the influential variables noted earlier, such as surface roughness.

Curve I – Curve IV were used in four sensitivity analyses for the simulation of heat flux to the LN_2 pool. Curve IV was developed as a part of this study using the experimental temperature histories recorded by T1 and T5 as a guide to modify the conventional boiling curves of LN_2. This new curve determines the heat flux to an LN_2 pool from an EH36 steel surface.

As demonstrated by Cowley et al. (Cowley et al. 1962), Allen (Allen 1966) and Leonhard et al. (Leonhard et al. 1967), placing a thin coating on a surface to be cooled down by a cryogenic liquid can significantly decrease the cooldown time. The reduction in the cooldown time depends on the coating material and thickness. For example, coating an Aluminium cylinder with 0.15 mm of

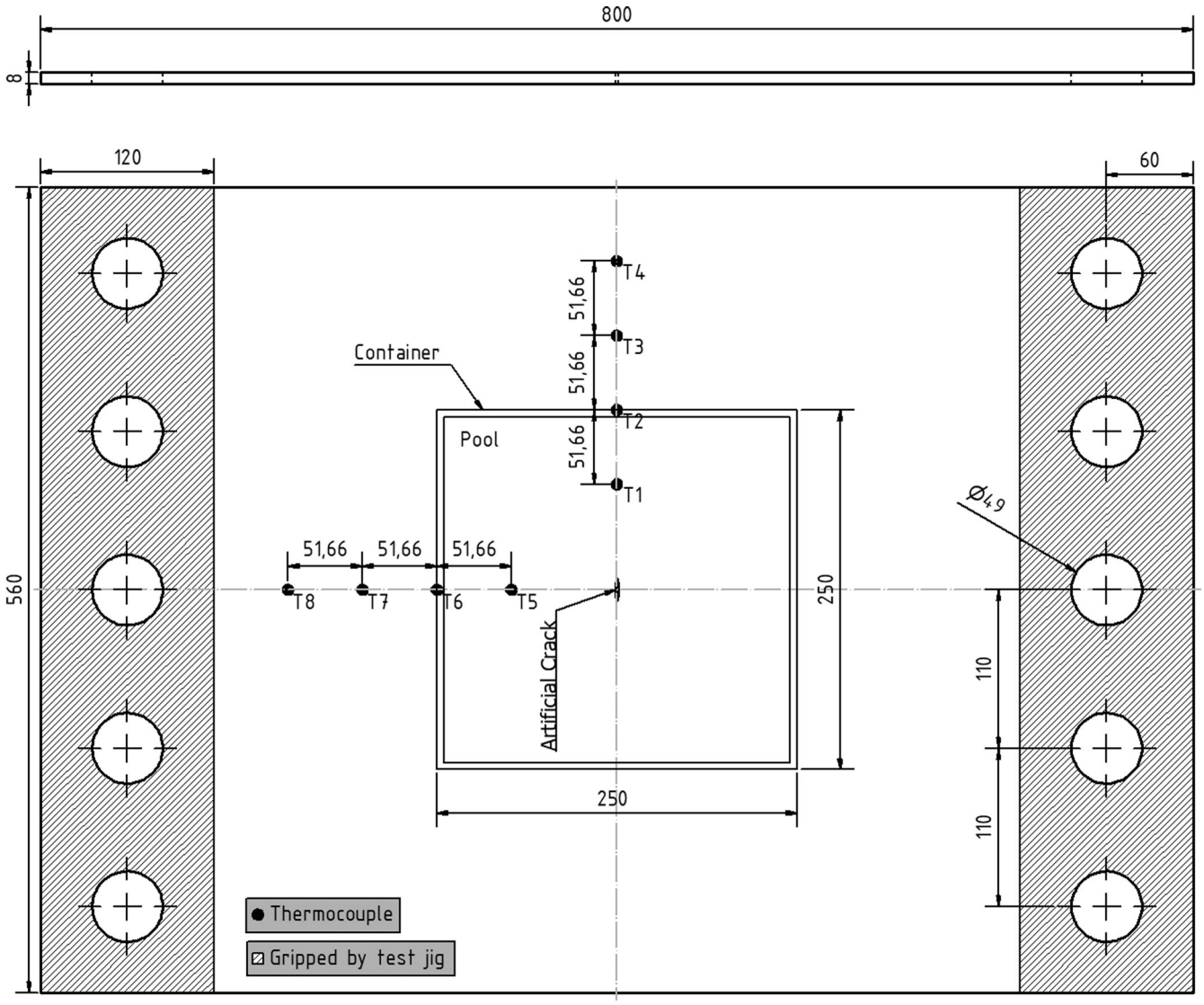

Figure 1. Specimen and container dimensions together with the location of thermocouples.

Vaseline diminished the cooldown time by 74% (Barron and Nellis 2017). Allen (Allen 1966) reported a 24% reduction in the cooldown time of coolant tubes when coated with Teflon. According to Sato's report in 1933 (Sato 1932), the large reduction in cooldown time results from a shortened film boiling regime due to a higher Leidenfrost point (earlier transition boiling). In line with these findings, for modelling heat flux to the liquid pool through the Al tape at Zone #2, Curve V was used. Curve V was obtained by shifting Curve IV to the right and by shortening the film boiling regime. The best agreement with the experimental results was achieved when a 50% shift to the right was applied with a smoother transition from the film boiling regime to the transition boiling regime.

3.2. Air convection

The average of the data collected by T9 showed that the air temperature drops almost linearly from 21 °C to −10 °C over the first 470 s of the test and remains almost unchanged afterwards (Equation (1)). These averaged data were used to simulate the air temperature at Zone #6. However, no thermocouple was placed to measure the air temperature near the top surface, and consequently, the temperature of the near-top-surface air was unknown. Hence, three different cases were considered to investigate the effect of air convection on the results:

(a) Adiabatic surface temperature for both Zone #4 and Zone #6.

(b) Air temperature history of Zone #4 is equal to that of Zone #6:

$$T_{a,ts} = T_{a,bs} = \begin{cases} -\dfrac{31}{470}t + 21, & t < 470 \\ -10, & t \geq 470 \end{cases} \quad (1)$$

(c) Air temperature at Zone #4 drops linearly during the film boiling regime until the critical temperature of nitrogen, −146.9 °C, is reached that is about when the film breaks at the centre of the pool and transition boiling initiates (t ≈ 220 s). Air temperature remains unchanged afterwards:

$$T_{a,ts} = \begin{cases} -\dfrac{167.9}{220}t + 21, & t < 220 \\ -146.9, & t \geq 220 \end{cases} \quad (2)$$

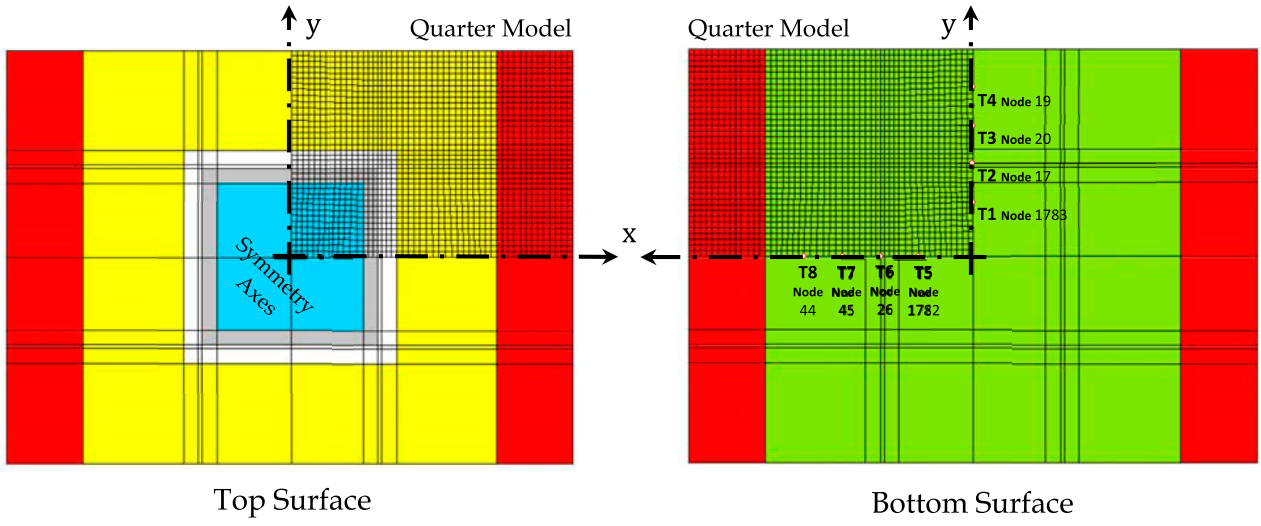

Zone #	Zone Colour	Zone Description	Zone Size
1		Direct heat flux to LN_2	$200\times200\ mm^2$
2		Indirect heat flux to LN_2 through Al tape	$(240\times240)-(200\times200)\ mm^2$
3		Adiabatic surface temperature	$(290\times290)-(240\times240)\ mm^2$
4		Air heat transfer – top surface	$(560\times560)-(290\times290)\ mm^2$
5		Grip parts heat supply	$4\left[(560\times120)-5(\pi\cdot24.5^2)\right]=4(560\times103.2)\ mm^2$
6		Air heat transfer – bottom surface	$560\times560\ mm^2$

Figure 2. Heat convection zones.

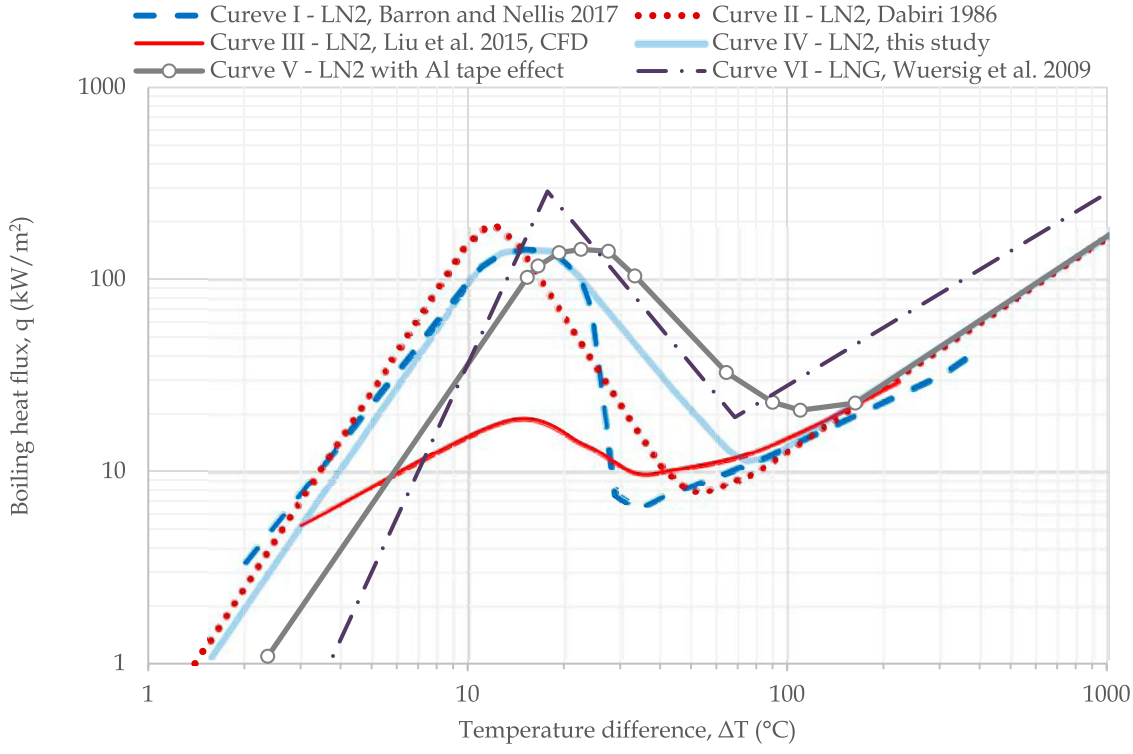

Figure 3. LNG and LN_2 heat flux curves.

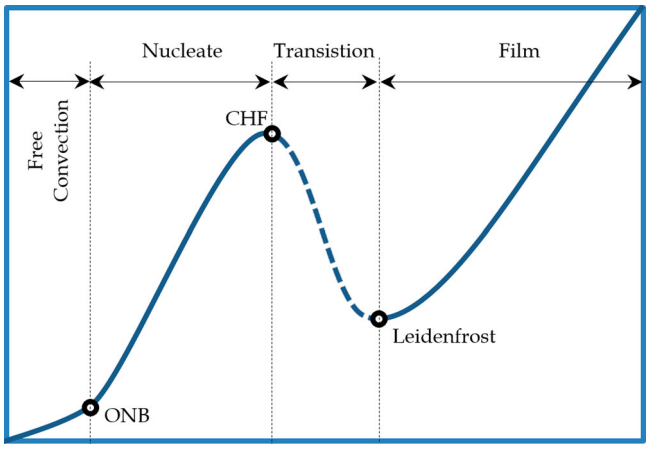

Figure 4. Typical boiling regimes (Carey 2008).

This case evaluates the effect of LN_2 vapour flow on the top surface. Similar to case (b), Equation (1) defines the air temperature for Zone #6.

It should be noted that, for simplification and due to the lack of experimental data, no gradient was considered for the air temperature although a large temperature gradient induced by the LN_2 vapour flow might have occurred for the near-top-surface air.

The dependency of air convection coefficient on surface-air temperature difference was defined using the following equation:

$$h_a = 0.061|T_s - T_a| + 8.7 \quad (3)$$

Equation (3) is based on observations and experimental data provided in (McQuiston et al. 2000) for bare steel pipes with different outer diameters, ranging from 12.7 mm to 127 mm, in still ambient air. This data was collected and presented in (McDonald et al. 2014) as 'heat transfer coefficient' versus 'temperature difference' graphs which showed a linear trend. McDonald et al. used these graphs in a mathematical model simulating the freezing time of water in steel pipes exposed to cold air. The mathematical model was successfully validated against experimental transient temperature data. To develop Equation (3) in the present study, the linear heat transfer graph for the largest pipe (127 mm) was used because, in (McDonald et al. 2014), the effect of pipe diameter on the heat transfer coefficient for pipes larger than 127 mm appears to be negligible. The heat transfer coefficient graphs presented by McDonald et al. showed that the effect of pipe diameter on the heat transfer coefficient decreases as the diameter increases, such that the difference between heat transfer coefficients for steel pipes with 114 and 127 mm diameters was equal to or less than 0.5%.

Given that the air temperature in the models studied herein could be higher or lower than the steel surface depending on time and location, the absolute value function was used in Equation (3). The typical natural convection coefficient of air at room temperature, for low surface-air temperature differences, is reported to be around 9 W/m^2 (Thomas 2002; Wang 2011; Gao et al. 2013; Kodur and Agrawal 2016; Roy et al. 2019; Thongchom et al. 2019). In the current study, for areas where the surface-air temperature difference is not significant (i.e. less than 10 °C), air convection coefficients calculated by Equation (3) fall between 8.7–9.3, which agree with those in the literature.

In Equation (3), T_s and T_a both change with time. T_a is input and can be calculated using Equation (1) and/or Equation (2), and T_s is computed in each increment when the finite element model is being solved. Therefore, h_a differs with time and location. To define this behaviour, a user subroutine in FORTRAN was developed which calculated and returned the value of h_a to the solver for each increment.

3.3. Grip parts heat supply

Referring to the experimental data in Part I, the temperatures recorded by T4 and T8 were different at the end of the test by about 12 °C to 45 °C for all specimens even though these thermocouples were located at the same distance from the plate centre. The temperature differences suggest a considerable heat supply from the grip parts of the hydraulic actuator. Subsequently, a convection coefficient of 250 W/m^2-K was considered for Zone #5 (four surfaces), which simulated the heat transfer between the grip parts and the steel surfaces. The temperature of the grip parts was considered to remain constant at 21 °C during the tests. In another case, the heat supply from grip parts was not taken into account to understand how it affected the numerical results. Table 1 sums up all the cases investigated in the current study.

3.4. Modelling EH36 steel plate

The steel plate with a thickness of 8 mm was modelled using 1296 linear quadrilateral elements of type DS4 in Abaqus. The size of each element was approximately 8 mm, which was found adequate through a mesh sensitivity analysis. Five integration points were used through the thickness given that the FE models were meant to be utilised for a coupled thermal-stress analysis in another study. Otherwise, three integration points would suffice for the thermal analysis. The total size of the steel plate is illustrated in Figure 2, including the mesh density of the quarter model. The side holes of the specimens were not modelled for simplification and computational efficiency. Instead, an equivalent width of 103.2 mm was considered for the gripped area (120 mm in the experimental specimens) so that the area in contact with grip parts in the numerical models was equal to that in the experiments.

3.4.1. Thermophysical properties of EH36 steel

EH36 steel thermophysical properties were given as functions of temperature. Equation (4) and Equation (5) define thermal conductivity (κ) and specific heat capacity (c_p) of EH36 steel, respectively. These functions were developed by Vilasboas et al. as a part of an ongoing research project at the Federal University of Bahia (Vilasboas 2019 (in brazilian portuguese)). They carried out a series of experimental studies to determine EH36 steel temperature-dependent thermophysical properties at low temperatures using an optimisation method. In this regard, the logarithmic model proposed by Marquardt at al. (Marquardt et al. 2002) was adopted to fit a logarithmic function to the conductivity and heat capacity data obtained from the experimental campaign. This resulted in the following formulations:

$$\log(\kappa(T)) = -1.0108(\log T)^2 + 5.1721(\log T) - 4.9013 \quad (4)$$

$$\log(\rho c_p(T)) = -0.3157(\log T)^2 + 2.0771(\log T) + 3.3667 \quad (5)$$

where ρ and T are EH36 steel density and temperature (in °K), respectively. Graphs of Equation (4), Equation (5) and thermal diffusivity ($\alpha = \frac{\kappa}{\rho c_p}$) in Figure 5 show that the conductivity and the heat capacity drop as the temperature decreases. With the temperature reduction, the drop rate increases similarly for both the conductivity and the heat capacity. As a result, diffusivity remains nearly constant in the temperature range recorded for the specimens during the pool boiling tests.

Table 1. Studied case scenarios.

Studied parameter	Case #	Boiling curve	Top-surface air temperature, $T_{a,ts}$ (°C)	Bottom-surface air temperature, $T_{a,bs}$ (°C)	Boiling curve used for Zone #2 (Al tape zone)	Convection coefficient of the grip parts (W/m^2-K)
Boiling curve	1	I	Adiabatic	Adiabatic	I	Adiabatic
	2	II	Adiabatic	Adiabatic	II	Adiabatic
	3	III	Adiabatic	Adiabatic	III	Adiabatic
	4	IV	Adiabatic	Adiabatic	IV	Adiabatic
Heat flux variations at the pool boundaries (Al tape effect)	5	IV	Adiabatic	Adiabatic	V	Adiabatic
Air convection	6	IV	Equation (1)	Equation (1)	V	Adiabatic
	7	IV	Equation (2)	Equation (1)	V	Adiabatic
Heat supply from grip parts	8	IV	Equation (2)	Equation (1)	V	h_{gp}=250

4. Results and discussion

In this section, temperature histories of nodes located at T1 to T8 positions are reported for all the studied cases (Cases #1 to #8). Table 1 shows the eight steps taken to develop a finite element model which best simulates the transient heat transfer process of the pool boiling tests, meaning that Case #8 produced the most accurate results. Figure 6, which compares the temperature histories obtained from Case #8 at T1 – T8 with those produced by the experimental studies, shows a good correlation between the numerical and experimental results. The effects of LN_2 boiling curve, air convective heat transfer, Al tape, and heat supply from grip parts on the FEA results are discussed in the next two sections using Case #8 as a reference.

4.1. Heat transfer analysis inside the pool boundaries – investigating LN_2 boiling curves

Compared to the other thermocouples, T1 and T5 were located close to the pool centre thereby not significantly affected by the heat transfer from the near-top-surface air, heat flux variations at the pool boundaries and the heat supply from grip parts. Thus, numerical temperature histories measured at T1 and T5 were selected to determine a boiling curve that could accurately simulate the heat flux to the LN_2 Pool. Comparing the first four cases in Figure 7, for which only the heat transfer between LN_2 and the steel surface was considered, there is no significant difference between the temperature histories when all four cases are in the film boiling regime. However, there is a large difference between them regarding the duration of the film boiling regime. Shortly after the onset of transition boiling, a sudden drop in temperature occurs which is successfully simulated by using Curves I, II and IV. However, Curve III (derived from a CFD simulation), which is relatively flat compared to the other curves, has failed to model the rapid temperature reduction during the transition and nucleate boiling regimes. Instead, the cooling during the transition and the nucleate boiling regimes continues with a slow rate comparable to that during the film boiling regime. The transition boiling for Case #1, Case #2 and Case #4 is reached in about 420, 400 and 260 s, respectively. All the temperature curves eventually flatten out at about −193 °C when a steady-state heat transfer is reached near the ONB point. The cooling times measured at T1 and T5 for Cases #1 to #4 are about 540, 500, 720 and 360 s, respectively.

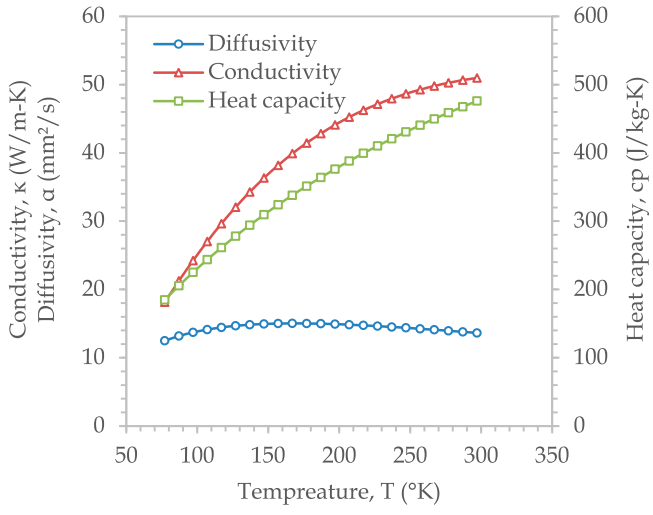

Figure 5. Conductivity, heat capacity and diffusivity of EH36 steel.

The boiling curve developed in the current study (Curve IV) assumes a higher Leidenfrost point compared to the conventional boiling curves resulting in an earlier transition from the film boiling regime, as observed in the temperature histories produced by Case #4. This might be induced by the surface roughness and the central crack of the steel plates utilised for the pool boiling tests. Also, the effect of the air convective heat transfer to the bottom surface is noticeable when Case #6 or #7 is compared to Case #4 or #5 in Figure 7. Clearly, having considered the heat transfer between the bottom surface and the air in the model, the Leidenfrost point has been shifted to a lower ΔT, closer to those observed in the conventional LN_2 boiling curves. This suggests that there might have been one or more secondary heat sources neglected during the derivation of the conventional heat flux curves. In other words, the effect of heat flux from a secondary heat source (such as air) might have been embedded in the conventional boiling curves. Nguyen et al. (Nguyen et al. 2020) also reported this shift to the right of the Leidenfrost point. However, their LN_2 pool was built on a concrete ground.

A comparison between the temperature histories from Cases #4 and #5 demonstrates that heat flux change near the pool boundaries caused by the Al tape has an insignificant impact on T1 and T5 temperature histories, which was projected earlier. Also, comparing Cases #7 and #8 with Case #6 shows that the thermal conditions considered for the near-top-surface air and the grip parts have negligible effects on T1 and T5 temperatures.

4.2. Heat transfer analysis at and outside the pool boundaries

In the previous section, the effect of boiling curves of liquid nitrogen as the primary heat exchange source on T1 and T5 temperature histories was investigated using Cases #1 to #4. Relative to the other boiling curves, Curve IV which was used for Case #4 could simulate a more accurate heat flux to the liquid pool. Consequently, Curve IV was adopted for Cases #5 to #8. These cases were developed to study the effects of the secondary heat exchange sources (i.e. the air and the grip parts) and the heat flux variations around the pool boundaries, mainly caused by the Al tape, on the FEA results.

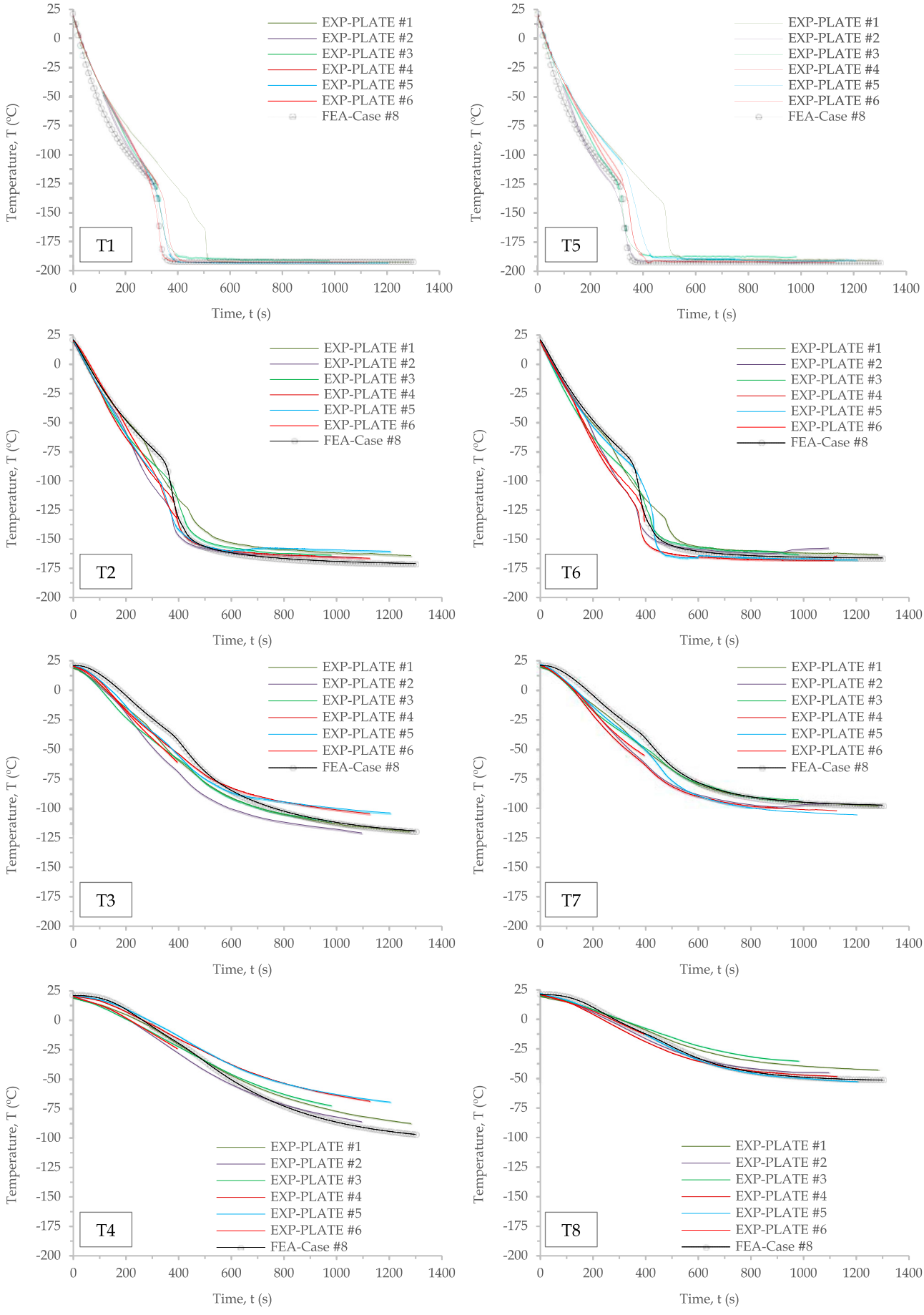

Figure 6. Comparison between experimental and numerical temperature histories.

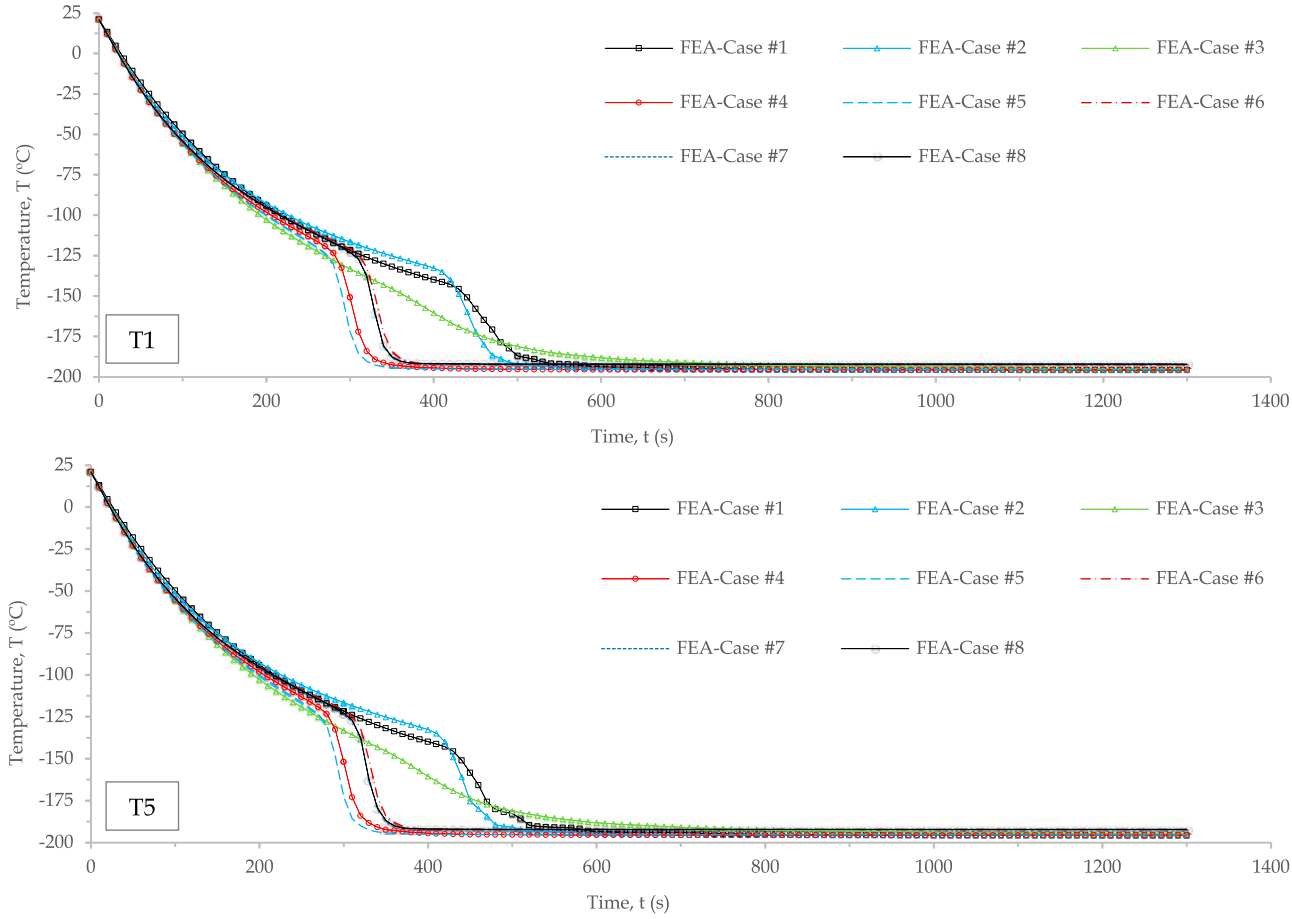

Figure 7. T1 and T5 temperature histories.

The results obtained from Cases #5 to #8 for T1 and T5, located inside the pool area, were discussed in the previous section. Hence, this section focuses on the temperature histories obtained for nodes located at and outside the pool boundaries (T2 to T4 and T6 to T8).

Figure 8 displays temperature histories of T2 to T4 and T6 to T8 for Cases #4 to #8. Simulating the effect of the Al tape in Case #5 via using Curve V for Zone #2 has slightly reduced the cooling time at T2 and T6 by about 50 s. The slight influence of the Al tape on the cooling rate decreases as the distance from the pool boundaries increases so that temperature histories recorded for T4 and T8 in Case #5 are not noticeably altered from those in Case #4. At the end of the simulation (t = 1300 s), Cases #4 and #5 have produced approximately the same temperature field meaning that the Al tape has almost no effect on the end results.

Having the air thermal convection included in the model has considerably influenced the FEA results. Although the thermal condition for the near-top-surface air was found uninfluential in the temperature histories of T1 and T5 (located inside the pool boundaries), it has significantly affected the temperature of the studied nodes located at and outside the pool boundaries (T2 – T4 and T5 – T8). According to Figure 8, Case #7 has improved the numerical results by considering a far lower temperature for the near-top-surface air than Case #6, whereas Case #6 has deteriorated the FEA results (for areas at and outside the pool boundaries). However, in Figure 7 it was observed that both Case #6 and Case #7 improved the FEA results for T1 and T5 locations. As noted earlier, this is because thermal conditions of the air at Zone #4 have a negligible impact on T1 and T5 located inside the pool boundaries. Comparing Case #7 with Case #5 in Figure 8, the impact of air convection on the FEA results increases with distance from the plate centre so that the largest difference occurs at T4 and T8. For T2, T3, T6 and T7, the temperature difference between the two cases is more prominent during the transition boiling (where the cooling rate has increased). At the end of the simulation, Cases #7 and #5 have produced very similar temperatures at all of the studied locations except for T4 and T8. Relative to Case #5, Case #7 has resulted in 10 and 16 °C lower temperatures at T4 and T8, respectively.

LN_2 vapour above the liquid surface can be as low as −194 °C (Sherman 1962). The LN_2 vapour temperature increases with distance from the liquid surface, but the rate and magnitude of this temperature increase were unclear in this study. However, the good agreement between the results from Case #7 and the experimental data suggests that the hypotheses listed in Table 1 for the air in Case #7 are plausible.

In Figure 8, only T7 and T8 temperatures are noticeably affected by the heat supply from grip parts, which was taken into account in Case #8, so that the end of simulation temperature at T8 has increased by 32% compared to Case #7. Temperature histories at the other studied locations are not influenced by the heat supply from grip parts. Therefore, the effect of the grip parts on the overall FETA results, required for a coupled thermal-stress analysis of the plate, could be neglected.

5. Conclusions

Eight different finite element models were developed to investigate the uncertainties involved in the FETA of marine steel structures

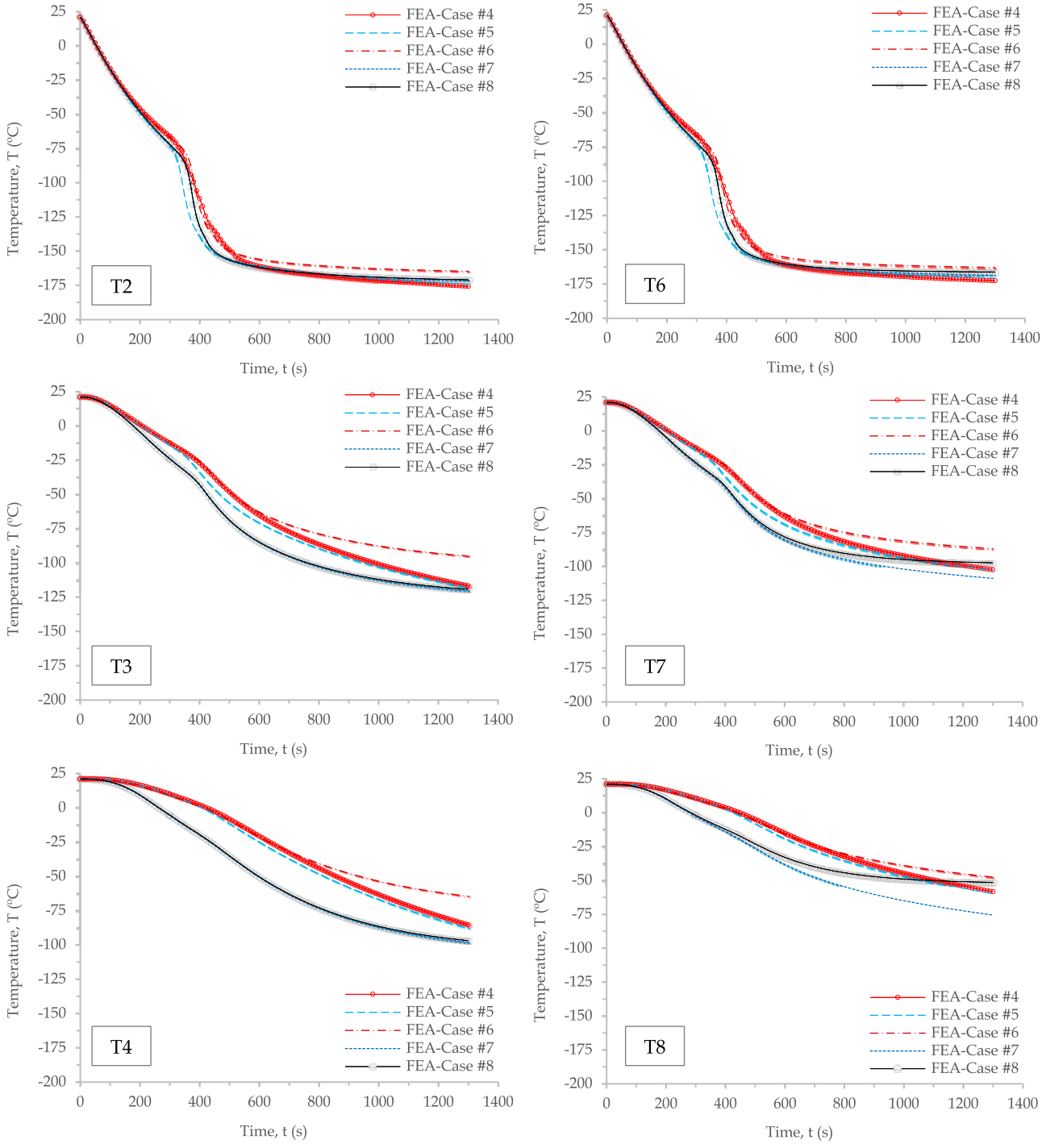

Figure 8. Temperature histories at and outside the pool boundaries (T2 – T4 and T5 – T8).

subject to local cryogenic spills. These models included an EH36 plate with six different convective heat transfer zones. The primary zone was located at the centre of the plate, simulating heat flux to a non-spreading LN_2 pool. Two novel temperature functions derived from experimental studies in cryogenic temperatures were employed to define thermal conductivity and heat capacity of EH36, which successfully modelled the conductive heat transfer through the steel plate. A user subroutine was developed in FORTRAN to define the convection coefficient of air as a function of surface-air temperature difference that changed with time and location.

Three different LN_2 boiling curves from the literature were studied, and a new heat flux curve for EH36 steel-LN_2 pool boiling was developed as a part of this study. The new heat flux curve produced the best agreement between the numerical and experimental results. This curve indicated a higher Leidenfrost point compared to the conventional LN_2 boiling curves, causing a shift to the right around the Leidenfrost point in the boiling curve. It was found that the lower Leidenfrost point in the conventional heat flux curves might have been caused by neglecting the effect of a secondary heat source. During the transient heat transfer phase, different boiling curves resulted in different temperature histories. However, when the steady-state heat transfer was reached, they produced almost the same temperature at the studied nodes located inside the pool boundaries.

A sensitivity analysis demonstrated that including the air convective heat transfer in the FETA noticeably changed the temperature field, and thus it is necessary for an accurate simulation. Two bilinear models in the subroutine defined the air temperature as a function of time for the top and the bottom surfaces. The best agreement with the experimental data was achieved when the temperature of the near-top-surface air was assumed to drop linearly to the critical temperature of nitrogen due to the LN_2 vapour flow on the top surface. This hypothesis considerably affected the temperature histories for the nodes located at and outside the pool boundaries so that a better agreement with the experimental results was achieved.

The Al tape and the heat supply from grip parts were found to have small effects on the temperature field required for a coupled thermal-stress analysis of the steel plate.

Overall, the close correlation between the numerical and the LN_2 pool boiling test results is promising, indicating that accurate finite element thermal analysis of marine structures subject to LNG spills is feasible.

Acknowledgements

The authors acknowledge the financial support of the Research Council of Norway through the Centers of Excellence funding scheme, project AMOS (Grant number 223254), and the Centers for Research-based Innovation funding scheme, project CASA (Grant number 237885), at the Norwegian University of Science and Technology.

The scientific contribution of Icaro Vilasboas, Danilo Gomes, and Armando Ribeiro from the Federal University of Bahia is highly appreciated.

Disclosure statement

No potential conflict of interest was reported by the author(s).

Funding

This work was supported by Norges Forskningsråd: [Grant Number 237885].

ORCID

Mojtaba Mokhtari http://orcid.org/0000-0002-1633-5919
Woongshik Nam http://orcid.org/0000-0002-9969-2574
Jørgen Amdahl http://orcid.org/0000-0002-3668-9896

References

Allen L. 1966. A method of increasing heat transfer to space chamber cryopanels. In: Advances in Cryogenic Engineering. Springer. p. 547–553.
Barron RF, Nellis GF. 2017. Cryogenic heat transfer. Boca Raton, FL: CRC press.
Carey V. 2008. Phenomena, liquid-vapor phase-change, 2nd ed. New York, NY, USA: Taylor & Francis Group.
Cowley C, Timson W, Sawdye J. 1962. A method for improving heat transfer to a cryogenic fluid. In: Advances in Cryogenic Engineering. Springer. p. 385–390.
Dabiri A. 1986. Liquid nitrogen cooling considerations of the Compact Ignition Tokamak. Fusion Technol. 10(3P2A):521–526.
Ehlers S, Østby E. 2012. Increased crashworthiness due to arctic conditions–The influence of sub-zero temperature. Mar Struct. 28(1):86–100.
Gao W, Dai J-G, Teng J, Chen G. 2013. Finite element modeling of reinforced concrete beams exposed to fire. Eng Struct. 52:488–501.
Kodur V, Agrawal A. 2016. An approach for evaluating residual capacity of reinforced concrete beams exposed to fire. Eng Struct. 110:293–306.
Leonhard K, Getty R, Franks D. 1967. A Comparison of Cooldown Time between Internally Coated and Uncoated Propellant Lines. In: Advances in Cryogenic Engineering. Springer. p. 331–339.
Liu Y, Olewski T, Véchot LN. 2015. Modeling of a cryogenic liquid pool boiling by CFD simulation. J Loss Prev Process Ind. 35:125–134.
Maddox J, Frederking T. 1966. Cooldown of insulated metal tubes to cryogenic temperatures. In: Advances in Cryogenic Engineering. Springer. p. 536–546.
Marquardt E, Le J, Radebaugh R. 2002. Cryogenic material properties database. In: Cryocoolers 11. Springer. p. 681–687.
McDonald A, Bschaden B, Sullivan E, Marsden R. 2014. Mathematical simulation of the freezing time of water in small diameter pipes. Appl Therm Eng. 73(1):142–153.
McQuiston FC, Parker JD, Spitler JD. 2000. Heating, ventilating, and air conditioning: analysis and design. New York: John Wiley & Sons.
Nam W, Hopperstad OS, Amdahl J. 2018. Modelling of the ductile-brittle fracture transition in steel structures with large shell elements: A numerical study. Mar Struct. 62:40–59.
Nam W, Mokhtari M, Amdahl J. 2021. Thermal analysis of marine structural steel EH36 subject to non-spreading cryogenic spills. Part I: experimental study. Ships Offshore Struct. 1–9.
Nguyen L-D, Kim M, Chung K. 2020. Vaporization of the non-spreading cryogenic-liquid pool on the concrete ground. Int J Heat Mass Transfer. 163:120464.
Paik JK, Lee DH, Noh SH, Park DK, Ringsberg JW. 2020. Full-scale collapse testing of a steel stiffened plate structure under axial-compressive loading triggered by brittle fracture at cryogenic condition. Ships Offshore Struct. 15 (sup1):S29–S45.
Roy K, Lim JB, Lau HH, Yong P, Clifton G, Johnston RP, Wrzesien A, Mei CC. 2019. Collapse behaviour of a fire engineering designed single-storey cold-formed steel building in severe fires. Thin-Walled Struct. 142:340–357.
Sato S. 1932. On the effect of 'facing' on the cooling velocity of a specimen during quenching.
Sherman J. 1962. Preservation of bull and human spermatozoa by freezing in liquid nitrogen vapour. Nature. 194(4835):1291–1292.
Thomas G. 2002. Thermal properties of gypsum plasterboard at high temperatures. Fire Mater. 26(1):37–45.
Thongchom C, Lenwari A, Aboutaha RS. 2019. Effect of sustained service loading on post-fire flexural response of reinforced concrete T-beams. ACI Struct J. 116(3):243–254.
Vilasboas I. 2019. (in brazilian portuguese). Determinação das propriedades térmicas do aço E36 pelo método inverso de transferência de calor Universidade Federal da Bahia.
Wang AJ. 2011. Studies on semi-continuous composite beams with non-uniform fire protection. Aust J Struct Eng. 12(1):29–46.
Wuersig G-M, GL JGA, Benjamin Scholz G, Maritime LSM. 2009. Effects of enveloping pool fires on LNG tank containment systems. Proceedings of the GasTech Conference: AbuDhabi, UAE.